

University of Groningen

Scalable, Template Driven Formation of Highly Crystalline Lead-Tin Halide Perovskite Films

Xi, Jun; Duim, Herman; Pitaro, Matteo; Gahlot, Kushagra; Dong, Jingjin; Portale, Giuseppe; Loi, Maria Antonietta

Published in:
Advanced Functional Materials

DOI:
[10.1002/adfm.202105734](https://doi.org/10.1002/adfm.202105734)

IMPORTANT NOTE: You are advised to consult the publisher's version (publisher's PDF) if you wish to cite from it. Please check the document version below.

Document Version
Publisher's PDF, also known as Version of record

Publication date:
2021

[Link to publication in University of Groningen/UMCG research database](#)

Citation for published version (APA):

Xi, J., Duim, H., Pitaro, M., Gahlot, K., Dong, J., Portale, G., & Loi, M. A. (2021). Scalable, Template Driven Formation of Highly Crystalline Lead-Tin Halide Perovskite Films. *Advanced Functional Materials*, 31(46), [2105734]. <https://doi.org/10.1002/adfm.202105734>

Copyright

Other than for strictly personal use, it is not permitted to download or to forward/distribute the text or part of it without the consent of the author(s) and/or copyright holder(s), unless the work is under an open content license (like Creative Commons).

The publication may also be distributed here under the terms of Article 25fa of the Dutch Copyright Act, indicated by the "Taverne" license. More information can be found on the University of Groningen website: <https://www.rug.nl/library/open-access/self-archiving-pure/taverne-amendment>.

Take-down policy

If you believe that this document breaches copyright please contact us providing details, and we will remove access to the work immediately and investigate your claim.

Downloaded from the University of Groningen/UMCG research database (Pure): <http://www.rug.nl/research/portal>. For technical reasons the number of authors shown on this cover page is limited to 10 maximum.

Scalable, Template Driven Formation of Highly Crystalline Lead-Tin Halide Perovskite Films

Jun Xi, Herman Duim, Matteo Pitaro, Kushagra Gahlot, Jingjin Dong, Giuseppe Portale, and Maria Antonietta Loi*

Low bandgap lead-tin halide perovskites are predicted to be candidates to maximize the performance of single junction and tandem solar cells based on metal halide perovskites. In spite of the tremendous progress in lab-scale device efficiency, devices fabricated with scalable techniques fail to reach the same efficiencies, which hinder their potential industrialization. Herein, a method is proposed that involves a template of a 2D perovskite deposited with a scalable technique (blade coating), which is then converted in situ to form a highly crystalline 3D lead-tin perovskite. These templated grown films are alloyed with stoichiometric ratio and are highly oriented with the (100) planes aligning parallel to the substrate. The low surface/volume ratio of the obtained single-crystal-like films contributes to their enhanced stability in different environments. Finally, the converted films are demonstrated as active layer for solar cells, opening up the opportunity to develop this scalable technique for the growth of highly crystalline hybrid halide perovskites for photovoltaic devices.

toxicity.^[5] Instead, divalent tin cation (Sn^{2+}) from the same group of the periodic table, gives rise to a similar cubic-like perovskite lattice and is considered to have a lower ecological impact.^[6] Thanks to a large number of activities in improving the fabrication methodology, the efficiencies of Sn perovskite solar cells have recently surpassed 10%.^[7–11] In spite of this astonishing development, Sn perovskites still suffer from oxidation under ambient conditions to Sn^{4+} state, which significantly hinders the long-term stability of devices.^[12,13]

In order to find a solution for the above-mentioned problems, Sn-alloyed perovskites, especially Sn-Pb binary ones (hereafter abbreviated as SnPb), have been proposed. Previous cradle-to-end analysis

(life-cycle assessment) suggested that the mixed SnPb perovskites potentially have a much lower environmental impact compared to other traditional photovoltaic semiconductors, like Si, copper indium gallium selenide (CIGS) and copper zinc tin sulfide (CZTS).^[14] Interestingly, the local chemical environments of Sn^{2+} encompassed by Pb^{2+} can strongly suppress oxidation, thus reinforcing the lattice stability.^[12] Importantly, the attractive advantage of such 3D perovskite is the tunable bandgap ranging from 1.2 to 1.6 eV, which is ideal for a bottom cell for all-perovskite tandem device.^[15] Meanwhile, the reduced bandgap close to the optimal wavelength for Shockley-Queisser (SQ) limit is expected to maximize the efficiency of single-junction solar cell through a balance of broad spectral absorption and minimal carrier relaxation losses.^[16]


By rationally designing the device layout, introducing low-dimensional structures and adding reducing agents, the state-of-the-art solar cells using narrow bandgap SnPb perovskites has been advanced enormously.^[17–21] In addition, mixed-cations lattice is used to replace mono-cation one to further improve device efficiency.^[18–21] However, to further push Sn-alloyed perovskites toward industrial production, the following fundamental issues should be addressed: i) Large-scale solution-based manufacturing methods should be investigated. Currently, a number of large-scale coating methods, including blade-coating, slot-die-coating and spay-coating, are designed to achieve highly efficient Pb perovskite devices.^[3] Nevertheless, progress in SnPb perovskites is lagging behind. The possible origin of such difficulty lies in the competing crystallization dynamics between the distinct Pb and Sn sublattices. Hence, mismatched nonstoichiometric binary lattices may be formed

1. Introduction

Over the past few years, the optoelectronic research community focusing on metal halide perovskites has grown spectacularly owing to the material's low-cost fabrication and exceptional properties.^[1–3] In particular, single-junction lead halide perovskite solar cells have reached a record efficiency of 25.5%, rivaling with the traditional single crystalline silicon devices.^[4] Nonetheless, the commonly used divalent lead cation (Pb^{2+}) poses major health and ecological concerns due to its inherent

J. Xi, H. Duim, M. Pitaro, K. Gahlot, M. A. Loi
Photophysics and OptoElectronics
Zernike Institute for Advanced Materials
University of Groningen
Nijenborgh 4, Groningen 9747 AG, the Netherlands
E-mail: M.A.Loi@rug.nl

J. Dong, G. Portale
Physical Chemistry of Polymeric and Nanostructured Materials
Zernike Institute for Advanced Materials
University of Groningen
Nijenborgh 4, Groningen 9747 AG, the Netherlands

 The ORCID identification number(s) for the author(s) of this article can be found under <https://doi.org/10.1002/adfm.202105734>.

© 2021 The Authors. Advanced Functional Materials published by Wiley-VCH GmbH. This is an open access article under the terms of the Creative Commons Attribution-NonCommercial-NoDerivs License, which permits use and distribution in any medium, provided the original work is properly cited, the use is non-commercial and no modifications or adaptations are made.

DOI: 10.1002/adfm.202105734

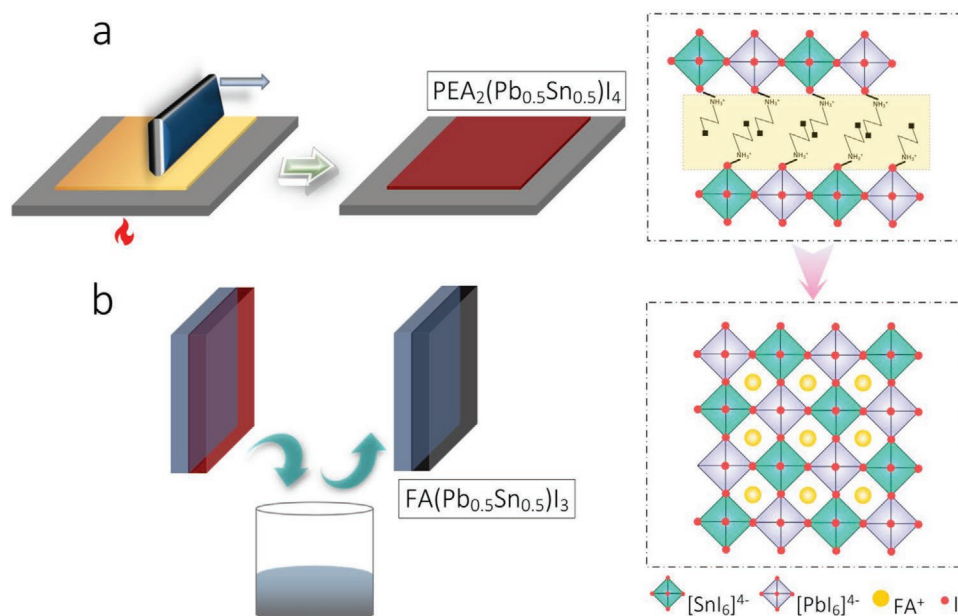


Figure 1. Fabrication process of layered-template $((\text{PEA})_2(\text{Pb}_{0.5}\text{Sn}_{0.5})\text{I}_4)$ driven $\text{FA}(\text{Pb}_{0.5}\text{Sn}_{0.5})\text{I}_3$ formation. a) Doctor-blade coated $((\text{PEA})_2(\text{Pb}_{0.5}\text{Sn}_{0.5})\text{I}_4)$ film and the corresponding lattice structure. b) Conversion of $((\text{PEA})_2(\text{Pb}_{0.5}\text{Sn}_{0.5})\text{I}_4)$ to $\text{FA}(\text{Pb}_{0.5}\text{Sn}_{0.5})\text{I}_3$ by in situ cation exchange reaction and the corresponding lattice structure.

when using large-scale coating methods. ii) With respect to the film crystallinity, a disordered polycrystalline state is typically obtained owing to the rapid nucleation especially in case of Sn compounds. The presence of a large density of grain boundaries contributes to a high surface/volume ratio. Recently, it was found that the activated corrosion that takes place at the perovskite surface dominates the degradation of SnPb perovskite polycrystalline films.^[22] For this reason, a stable SnPb perovskite film should have a minimized surface/volume ratio, approaching the situation of a single-crystal-like film quality.

It is worth noting that 2D layered perovskites, in which large organic spacers are periodically inserted along certain planes, are revisited as an option to partially replace 3D ones for better stability.^[9,20,23–26] The 2D structure can be readily formed with high crystallinity by different fabrication techniques.^[27] Furthermore, we previously reported that the layered lattice can work as an ordered platform for the in-situ growth of Pb-based 3D lattices via a nondestructive cation exchange reaction.^[28] Therefore by extrapolation, supposing that layered SnPb perovskites can be formed by a scalable method, single-crystal-like 3D SnPb films could then be obtained through a simple cation exchange procedure.

Here we demonstrate the formation of high-quality 3D SnPb perovskite films converted from a layered-template fabricated with the scalable blade coating. In our procedure, a prototypical Ruddlesden-Popper 2D perovskite $(\text{PEA})_2(\text{Pb}_{0.5}\text{Sn}_{0.5})\text{I}_4$ (PEA = 2-phenylethylammonium) was first blade-coated as the layered-template, subsequently the PEA cations were in-situ exchanged by the formamidinium (FA) cations to obtain the 3D perovskite $\text{FA}(\text{Pb}_{0.5}\text{Sn}_{0.5})\text{I}_3$. With this procedure the crystallinity and stoichiometry of the converted 3D perovskites can be easily controlled. The detailed characterization of the optimized $\text{FA}(\text{Pb}_{0.5}\text{Sn}_{0.5})\text{I}_3$ films revealed their high crystallinity

and preferred orientation with the (100) planes parallel to the substrate. Instead, spin-coated $\text{FA}(\text{Pb}_{0.5}\text{Sn}_{0.5})\text{I}_3$ films prepared with solutions of the same concentration showed poor crystallinity with randomly oriented grains.

Besides being highly oriented with respect to the substrate, the converted films showed significantly enhanced photoluminescence. More importantly, the converted sample demonstrated increased stability in comparison to the spin-coated one under different testing environments. This increased stability can be attributed to the reduced surface degradation determined by the smaller surface/volume ratio respect to polycrystalline films. Finally, we verified that the converted $\text{FA}(\text{Pb}_{0.5}\text{Sn}_{0.5})\text{I}_3$ films even if not fully optimized for solar cell fabrication, give rise to devices with near 10% efficiency, which at the opposite of the spin coated control sample, showed stable efficiency under light soaking in N_2 for 24 h. We believe this is a first step toward the fabrication with scalable techniques of single-crystal-like 3D Sn-alloyed perovskites optoelectronic devices.

2. Results and Discussion

Figure 1 illustrates the fabrication procedure for the layered-template (LT) growth of $\text{FA}(\text{Pb}_{0.5}\text{Sn}_{0.5})\text{I}_3$ films. The details of the sample fabrication can be found in the experimental section, it is important to underline that all our samples contain SnF_2 in the precursor solutions, as the addition of this reducing agent is indispensable to avoid the solution aging induced by dimethyl sulfoxide (DMSO) (Figure S1, Supporting Information). The whole process is described as follows: i) $(\text{PEA})_2(\text{Pb}_{0.5}\text{Sn}_{0.5})\text{I}_4$ films were coated by an optimized doctor-blade procedure. We observed that the amount of DMSO in the precursor solution is critical for the film crystallinity

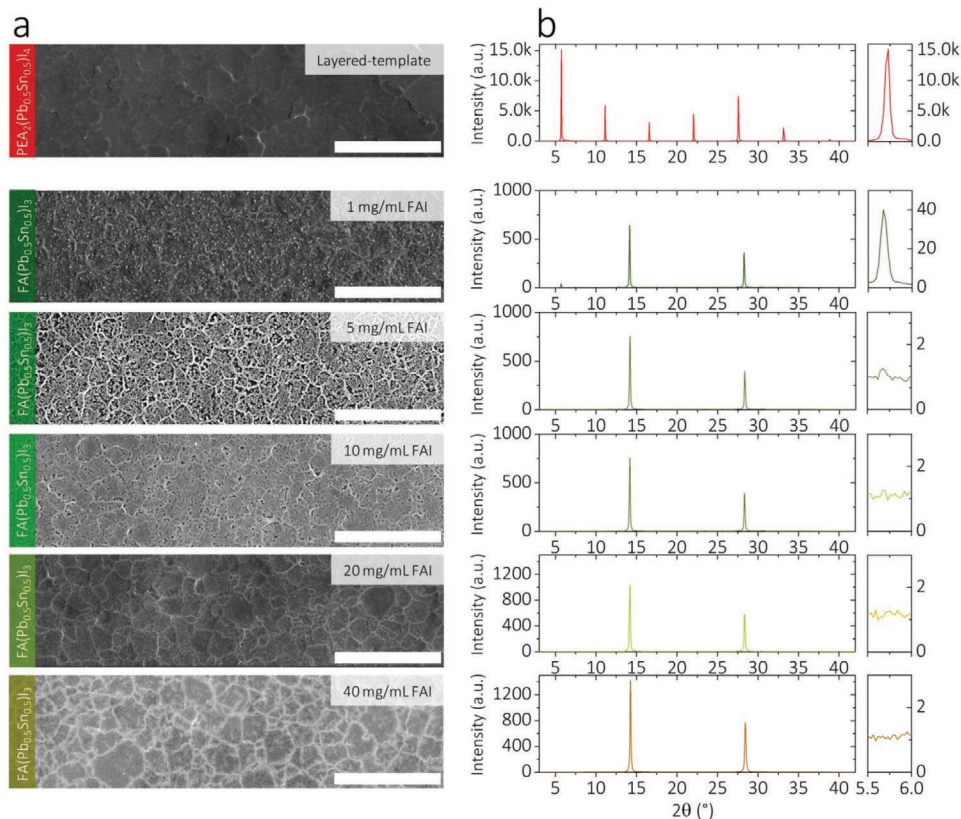


Figure 2. LT $\text{FA}(\text{Pb}_{0.5}\text{Sn}_{0.5})\text{I}_3$ formation by cation exchange reaction. a) SEM images (scale bar: 50 μm) and b) XRD patterns of the LT $\text{FA}(\text{Pb}_{0.5}\text{Sn}_{0.5})\text{I}_3$ films converted using FAI solutions of different concentrations (right panel denotes (200) plane in $(\text{PEA})_2(\text{Pb}_{0.5}\text{Sn}_{0.5})\text{I}_4$).

(Figure S2, Supporting Information). When equimolar DMSO and metal iodides (PbI_2 and SnI_2) were used, the crystallinity appeared to be well controlled. This can be attributed to the intermediate roles of DMSO- $(\text{PbI}_2/\text{SnI}_2)$ Lewis adducts during crystallization.^[29] ii) The obtained $(\text{PEA})_2(\text{Pb}_{0.5}\text{Sn}_{0.5})\text{I}_4$ films were dipped into FAI solutions to be in-situ converted to $\text{FA}(\text{Pb}_{0.5}\text{Sn}_{0.5})\text{I}_3$ films via cation exchange. The large grains of the template 2D films were well-preserved in the resulting 3D films (Figure S3, Supporting Information). In the case of very large grains, cracks appeared on the surface dividing the grains into smaller sub-grains. iii) The converted $\text{FA}(\text{Pb}_{0.5}\text{Sn}_{0.5})\text{I}_3$ films were washed with isopropanol, and then dried by spinning at room temperature.

Using scanning electron microscopy (SEM) and X-ray diffraction (XRD), we systematically investigated the influence of the FAI concentration on the film quality obtained through the cation exchange reaction, as shown in **Figure 2** and Figure S4 (Supporting Information). Before exchange, the blade-coated $(\text{PEA})_2(\text{Pb}_{0.5}\text{Sn}_{0.5})\text{I}_4$ films show a homogeneous compact morphology, which have a well-defined layered structure with periodically aligned $(00k)$ planes parallel to the substrates. During the exchange process, as the FAI concentration increase from 1 to 10 mg mL^{-1} , the coverage of the converted $\text{FA}(\text{Pb}_{0.5}\text{Sn}_{0.5})\text{I}_3$ grains is progressively improved. Simultaneously, (100) and (200) planes from the emerging 3D cubic lattice become stronger, while the (002) plane belonging to the layered structure gradually disappears, as shown in Figure 2b. This observa-

tion verifies that a cation exchange reaction occurred between PEA^+ and FA^+ . As the FAI concentration further increases to 20 mg mL^{-1} and even 40 mg mL^{-1} , full coverage of 3D perovskite grains is obtained with high crystallinity of the resulting film. For the concentrations above 1 mg mL^{-1} , no traces of the layered perovskites could be observed in the XRD pattern. Hence, a completely converted high-quality $\text{FA}(\text{Pb}_{0.5}\text{Sn}_{0.5})\text{I}_3$ film can be produced. Notably, as the FAI concentration increases, we observe a monotonic shift of the (200) peaks to larger diffraction angles (Figure S5, Supporting Information). The band edges also move toward lower energy (Figure S6, Supporting Information). Considering the different cation exchange rates of the Sn- and Pb-sublattice, the variation in the lattice parameter and band gap could be due to the formation of FAPbSnI_3 with ideal Sn/Pb stoichiometry at high FAI concentrations. This is rather different with respect to what we observed in case of pure Pb compounds.^[28] We further reveal that the absorbance intensity of the converted film can be readily controlled by varying the blade speed in the deposition of the 2D templating film (Figure S7, Supporting Information). By comparison, the $\text{FA}(\text{Pb}_{0.5}\text{Sn}_{0.5})\text{I}_3$ films converted from a spin-coated 2D template show a poor morphology with plenty of pinholes (Figure S8, Supporting Information).

After the optimization of the cation exchange process, we aim at understanding the structural properties of the converted $\text{FA}(\text{Pb}_{0.5}\text{Sn}_{0.5})\text{I}_3$ films. For comparison, a spin-coated (SP)

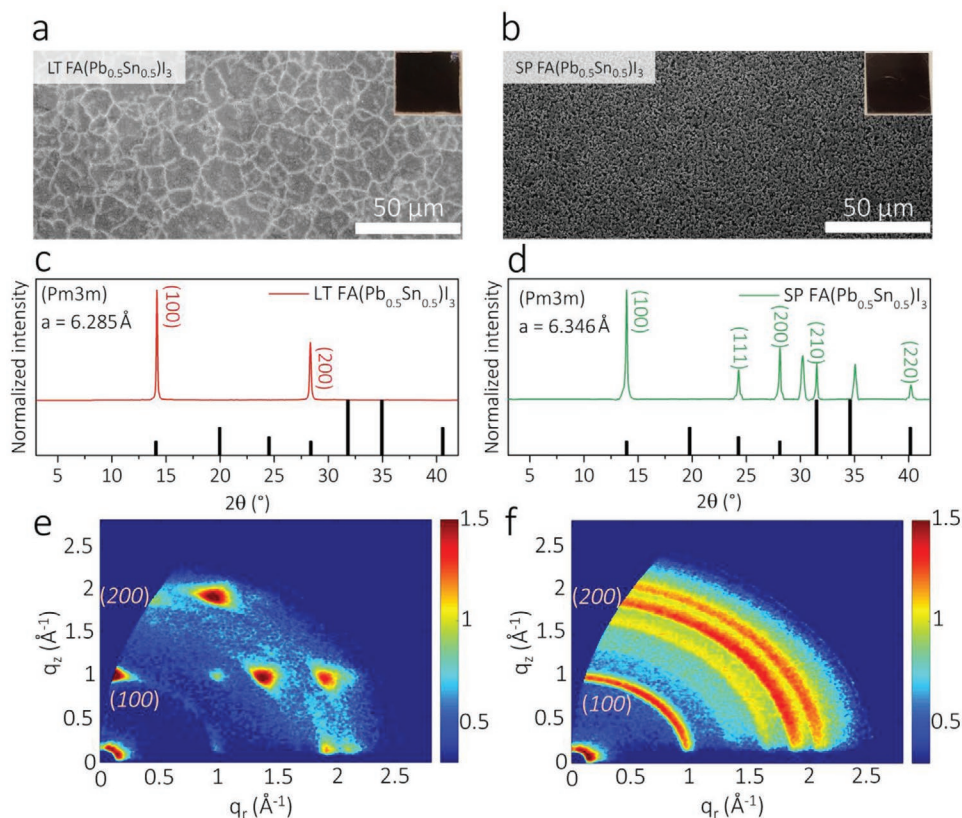


Figure 3. Crystal structures of LT and SP FA(Pb_{0.5}Sn_{0.5})I₃ films. a,b) SEM images, insets are the photographs of LT and SP FA(Pb_{0.5}Sn_{0.5})I₃ films. c,d) Refined XRD patterns (black lines index to the fitted (hkl) planes) and e,f) GIWAXS patterns.

FA(Pb_{0.5}Sn_{0.5})I₃ film was made using the same molar concentration as the doctor bladed one. **Figure 3** summarizes the overall morphological and structural properties of these two samples. High-magnification SEM images can be found in Figure S9 (Supporting Information). Unlike the superb surface and crystal quality of LT sample, SEM image reveal that the SP film exhibits a poor surface coverage and is made of rather small crystalline grains. This is typical considering the uncontrolled nucleation and fast coarsening during spinning. In addition, mismatched nonstoichiometric structures can form easily when directly depositing alloyed 3D perovskite from their precursor solutions. The high-quality morphology of LT film is verified by atomic force microscopy (AFM) images in which micrometer-sized grains are observed (Figure S10, Supporting Information). Refined normalized XRD patterns (Figure 3c,d) uncovers that the two films share the similar cubic lattice in the *Pm3m* space group (see zoomed original diffraction peaks in Figure S11, Supporting Information). Interestingly, the LT lattice has a smaller unit cell ($a = 6.285 \text{ \AA}$) than the SP lattice ($a = 6.346 \text{ \AA}$), indicating that a stoichiometry closer to the predicted binary composition ($a = 6.298 \text{ \AA}$)^[30] is obtained through the cation exchange reaction. More importantly, the diffraction patterns of the two types of films differ a lot. For LT FA(Pb_{0.5}Sn_{0.5})I₃, only diffraction peaks arising from the (100) and (200) planes are observed, as an indication of the highly oriented crystalline structure. For the SP film, additional peaks corresponding to the (111), (210), and (220) planes appear due to the random orientation of the crystalline grains.

Grazing-incidence wide-angle X-ray scattering (GIWAXS) was used to further unveil the structural properties and assess the texture of the films. The results of these measurements are shown in Figure 3e,f. In Figure S12 (Supporting Information), the extracted GIWAXS profiles are given. The GIWAXS profile for the LT sample (Figure 3e) clearly shows a highly oriented crystalline structure, with the (100) planes aligning parallel to the substrate. For the SP sample (Figure 3f), distinct Debye–Scherrer rings emerge instead, implying random orientation of the crystallites. Thus, the LT FA(Pb_{0.5}Sn_{0.5})I₃ film obtained by cation exchange retains the strongly textured structure characteristic of the 2D template.

Next, we aim to understand the differences of physical properties of the two FA(Pb_{0.5}Sn_{0.5})I₃ films. The full width at half maximum (FWHM) of the (100) diffraction in the unrefined original XRD pattern (Figure 4a) is estimated to 0.122° and 0.164° for LT and SP sample, respectively, showing the significantly enhanced crystallinity using the LT rather than SP method. The UV–vis absorption spectra (Figure 4b) reveal a higher absorbance for LT sample across the entire spectrum, mainly owing to its larger thickness ($\approx 260 \text{ nm}$) and better homogeneity than that ($\approx 150 \text{ nm}$) of SP sample made with the same molarity of precursors. This difference should be attributed by the different crystallization mechanism: Blade-coating method allows an outward horizontal growth along the blade direction, whereas spin-coating method entails a top-to-bottom downward growth direction.^[31,32]

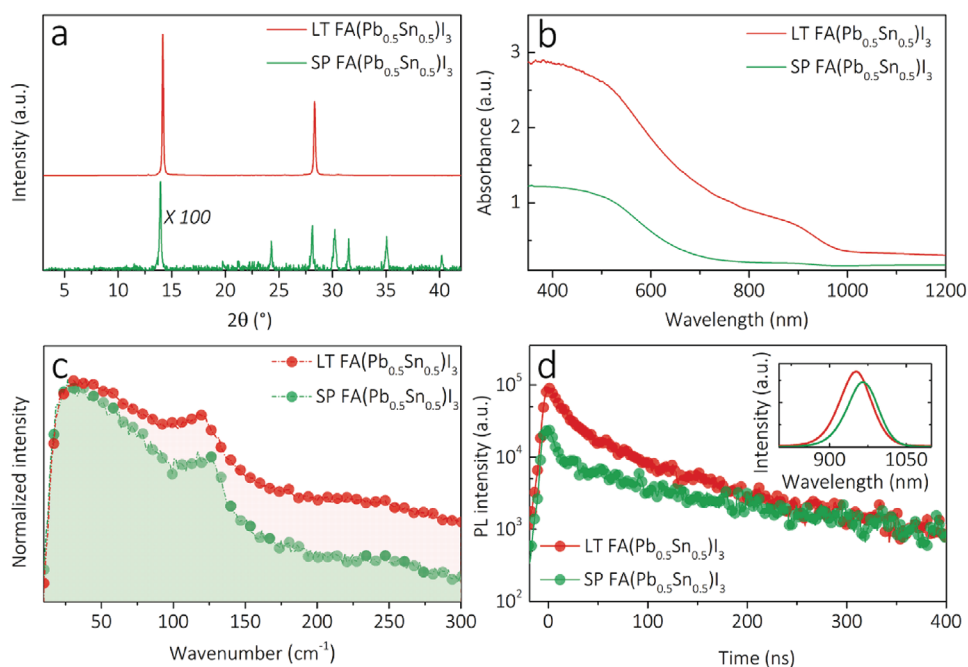


Figure 4. Comprehensive properties of parallel LT and SP $\text{FA}(\text{Pb}_{0.5}\text{Sn}_{0.5})\text{I}_3$ films. a) Unrefined original XRD patterns, b) UV-vis absorption spectra, and c) normalized nonresonant Raman spectra. d) As collected time-resolve PL decay of the two $\text{FA}(\text{Pb}_{0.5}\text{Sn}_{0.5})\text{I}_3$ films with a same thickness (≈ 260 nm) (inset: steady-state PL spectra were averaged by the collected data from five different randomly selected spots (beam diameter of roughly $200 \mu\text{m}$) of the films in N_2).

When focusing on the band edges of the spectra (Figure S13, Supporting Information), we noticed that the LT film possesses a smaller optical band gap (1.257 eV) compared to that of the SP film (1.286 eV). This difference in the band gap could be a sign of the reported different unit cell size and different Pb/Sn ratio obtained with the two methods. In general, for SnPb binary perovskites, the valence band maximum is composed of Sn-5s and I-5p orbitals, whereas the conduction band minimum is mainly determined by Pb-6p orbitals.^[14] Since the unit cell of the LT lattice is slightly smaller than that of SP lattice, the overlap of Sn-5s and I-5p orbitals is expected to increase, resulting in an up shifted valence band and narrower bandgap. As expected, the strong excitonic peak at around 600 nm observed for the blade-coated $(\text{PEA})_2(\text{Pb}_{0.5}\text{Sn}_{0.5})\text{I}_4$ film (Figure S14, Supporting Information) totally disappear in LT $\text{FA}(\text{Pb}_{0.5}\text{Sn}_{0.5})\text{I}_3$, implying a complete 2D-3D conversion in line with the observation from XRD.

Figure 4c shows the representative normalized nonresonant Raman spectra excited by a laser source of 532 nm. The original Raman data obtained from different spots and wide-field images of the films are given in Figure S15 (Supporting Information). A single peak at around 120 cm^{-1} is identified for both samples, which can be assigned to the pronounced M-I (M denotes Pb/Sn) stretching mode from 3D $[\text{MI}_6]^{4-}$ octahedral units. Meanwhile, the distinct low-wavenumber peaks (55 cm^{-1}) dominating the 2D perovskite (Figure S15, Supporting Information) are absent for LT $\text{FA}(\text{Pb}_{0.5}\text{Sn}_{0.5})\text{I}_3$ film. When comparing the Raman spectra of the LT and SP films, it appears that the dominant Raman peak of the SP sample is located at slightly higher wavenumber than that of the LT film. This could result from a change in the lattice's vibrational modes due to the Sn-deficient composition of the SP lattice. Moreover, both samples

exhibit uniform photoluminescence (PL) distribution with only small point-to-point variations in the intensity (Figure S16, Supporting Information). Time-resolved photoluminescence (PL) measurements (Figure 4d) additionally reveal a significant difference in the charge carrier dynamics of the SP and LT films. While the SP film shows a nearly mono-exponential behavior with a slight fast decay component, the LT film shows a clear bi-exponential decay. The difference in charge carrier dynamics mainly manifests itself in an increased instantaneous PL intensity of the LT as compared to the SP film, which we argue most likely stems from a fast trapping of charge carriers in the SP film that takes place on a timescale shorter than the temporal resolution employed here. At longer delay times (>200 ns), the intensity and decay rate are very similar for both films and is determined by the bimolecular recombination of charge carriers. A similar trend is observed in the steady state spectra obtained from these films (inset Figure 4d), for which the PL intensity of the LT was indeed slightly higher than that of the SP film. In addition, the SP film shows a clear redshift (corresponding to a larger Stokes shift) with respect to the LT film, which is suggestive of a larger trap state density in the former. Consequently, the high quality LT $\text{FA}(\text{Pb}_{0.5}\text{Sn}_{0.5})\text{I}_3$ film can be a potential candidate for high performance photovoltaics.

In order to examine the stability of above samples, we stored them for the same period of time in three different environments, namely, under 1 sun light soaking (nitrogen glove box), in ambient air ($\approx 50\%$ humidity), and at high temperature (160°C in nitrogen glove box). i) In the light soaking condition (18 h), the crystallinity of each sample could be maintained well (Figure 5a,b). This result indicates that 3D SnPb perovskites are fundamentally illumination resistant, irrespective of slight

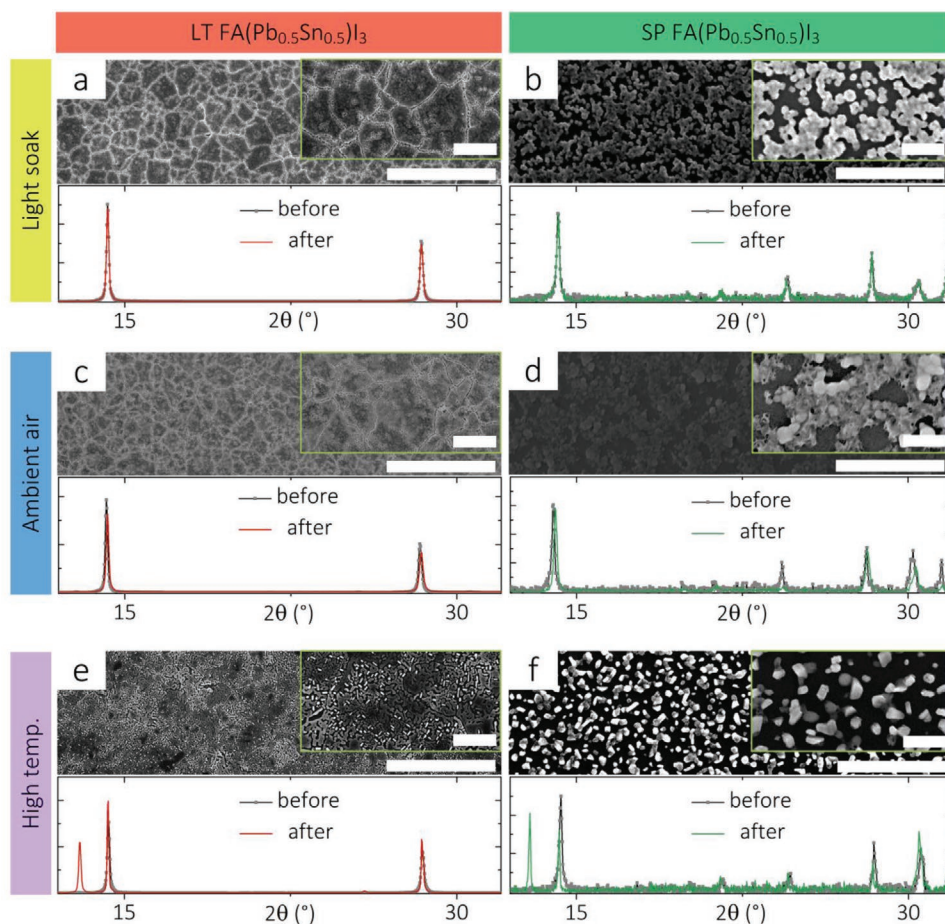


Figure 5. Stability of LT and SP $\text{FA}(\text{Pb}_{0.5}\text{Sn}_{0.5})\text{I}_3$ films evaluated by SEM and XRD. a, b) 1 sun light soaking for 18 h (nitrogen glove box), c, d) ambient air for 24 h ($\approx 50\%$ humidity), and e, f) high temperature for 8 h (160°C). SEM images correspond to the samples after aging (note: SEM images in Figure 3 are taken on fresh samples), and XRD patterns correspond to the samples before and after aging. Scale bar in low- and high-magnified SEM images for LT film: $50\ \mu\text{m}$ and $10\ \mu\text{m}$, and in low- and high-magnified SEM images for SP film: $10\ \mu\text{m}$ and $2\ \mu\text{m}$.

differences in their lattice structure and composition. Hence, $\text{FA}(\text{Pb}_{0.5}\text{Sn}_{0.5})\text{I}_3$ is a very good light absorber for solar cells. ii) In ambient conditions (24 h), the LT sample is more stable than SP sample (Figure 5c,d). After storage, some irregularities emerge on LT grain surfaces, while a great deal of newly formed sphere-like features appear between the grains of the SP film and interconnect them. Since the sample surfaces were exposed to oxygen-rich atmosphere, solid SnO_2 and volatile I_2 are expected to be the main degradation products.^[11] For the degraded SP sample, the reason for the evident variation of film morphology could be the formation of SnO_2 . Accordingly, the (100) peak in the XRD pattern moves to a higher diffraction angle for SP sample, different from what occurs in LT sample, where the diffraction features are almost unchanged. This comparison clearly demonstrates the improved air stability of the LT film. iii) In the high temperature condition (8 h), both samples degenerated but in a different degree (Figure 5e,f). For the LT film, a part of the original crystals evolves into smaller rod-like crystals. However, for the SP sample, the whole film is divided into discontinuous crystals with much decreased surface coverage. The produced new material for each degraded sample

results from PbI_2 formation, verified by the emergence of peaks assigned to (001) plane of the PbI_2 hexagonal lattice. The relative ratios between the intensity of the (001) peak of formed PbI_2 phase and the (100) peak of remaining $\text{FA}(\text{Pb}_{0.5}\text{Sn}_{0.5})\text{I}_3$ in the degraded LT and SP sample are estimated to be 0.55 and 1.31, respectively. This unveils that the high temperature degradation rate of SP sample is more than twice than that of the LT one. Hence, the LT sample is recognized to be more stable also to high temperature treatments. In summary, compared to the generally used SP process, the proposed LT approach leads to intrinsically more stable $\text{FA}(\text{Pb}_{0.5}\text{Sn}_{0.5})\text{I}_3$ film.

Given the encouraging properties of the LT $\text{FA}(\text{Pb}_{0.5}\text{Sn}_{0.5})\text{I}_3$ films, we attempted to fabricate solar cells to test whether their improved quality makes them promising candidates for applications. With respect to the device structure, a typical inverted planar architecture was adopted here, composed of indium tin oxide (ITO)/poly(3,4-ethylenedioxythiophene):polystyrene sulfonate (PEDOT:PSS) (30 nm)/ $\text{FA}(\text{Pb}_{0.5}\text{Sn}_{0.5})\text{I}_3/\text{C}_{60}$ (60 nm)/2,9-dimethyl-4,7-diphenyl-1,10-phenanthroline (BCP) (6 nm)/Al (100 nm) (Figure 6a). The detailed process of device fabrication can be found in the experimental section. Here it is important

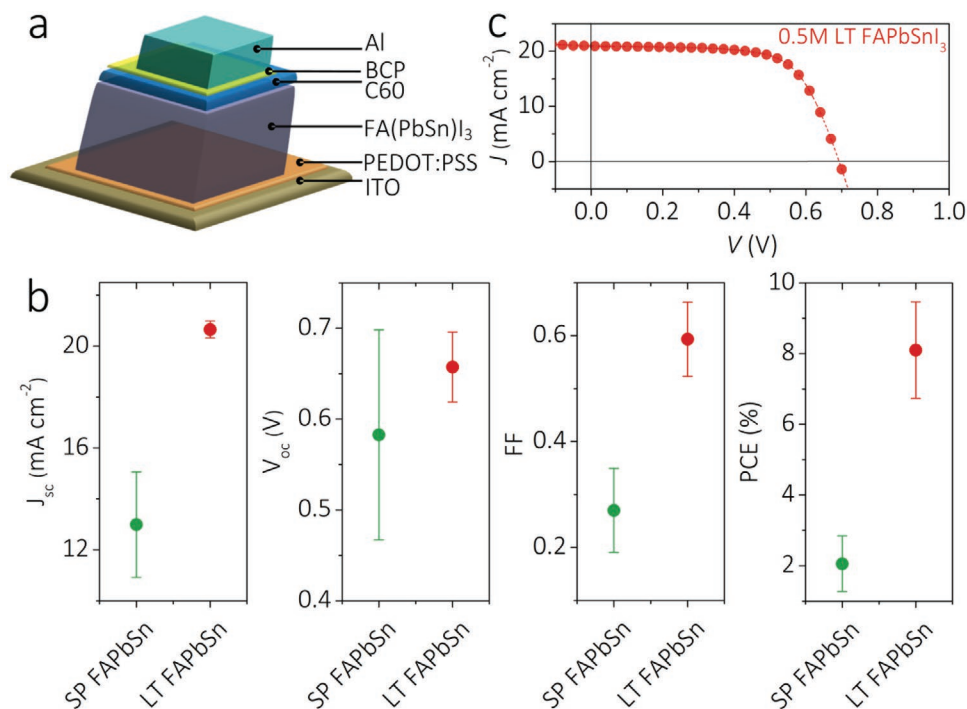


Figure 6. Inverted planar solar cells using LT and SP FA(Pb_{0.5}Sn_{0.5})I₃ films fabricated using 0.5 M precursor solutions. a) Device structure, b) statistical parameters (8 cells) of the photovoltaic performance and c) *J*-*V* curves of the best performing solar cells.

to underline that a significant challenge is represented by the numerous cracks affecting the otherwise exceptional quality of the thin films. A vacuum evaporated C₆₀ film (60 nm) was selected as the electron transporting layer, owing to its generally uniform morphology and advantage of solvent-free deposition. An ultrathin BCP film (6 nm) worked as a hole blocking layer. Figure 6b summarizes the statistical parameters of the photovoltaic performance in the devices made by LT and SP films. The LT films give rise to much higher and more reproducible device parameter than SP films. Here we should emphasize that the SP film was fabricated using a low-concentration equimolar (0.5 M) solution analogous to the solutions used to fabricate the LT films, it therefore shows performances that are far from the one of optimized spin-coated devices.

In detail, the statistical short-circuit current density (*J*_{sc}), open-circuit voltage (*V*_{oc}), fill factor (FF), and power conversion efficiency (PCE) for LT-based devices are (20.64 ± 0.33) mA cm⁻², (0.66 ± 0.04) V, (0.59 ± 0.07), and (8.01 ± 1.36)%, respectively. In contrast, SP-based devices fabricated with a 0.5 M solution yield much lower values for *J*_{sc}, *V*_{oc}, FF, and PCE of (12.99 ± 2.07) mA cm⁻², (0.58 ± 0.11) V, (0.27 ± 0.08), and (2.06 ± 0.78)%, respectively. In addition, SP-based devices fabricated with the same thickness of the LT sample (≈260 nm) show a slightly improved PCE to (3.26 ± 0.41)% (Figure S17, Supporting Information) with respect to SP devices fabricated using 0.5 M, which is still far from LT-based devices. The significantly enhanced device performance using LT film benefits from the profoundly improved charge-carrier transport in the highly oriented and closely packed crystal grains. The maximum power point (MPP) tracking tests (Figure S18, Supporting Information)

reveal that LT-based devices have larger stability under light soaking. While SP-based devices show an obvious decline of efficiency after about 12 h, while LT-based one displayed a slight increase of efficiency until 24 h. Figure 6c shows the *J*-*V* curves of the best performing devices. Encouragingly, the LT-based champion device exhibits promising *J*_{sc}, *V*_{oc}, FF, and PCE of 20.99 mA cm⁻², 0.69 V, 0.67, and 9.77%. The integrated short-circuit current density (20.83 mA cm⁻¹) obtained from the EQE spectra (Figure S19, Supporting Information) is similar to the one (20.99 mA cm⁻¹) measured under AM1.5G from *J*-*V* curves, verifying the reliability of *J*_{sc}. Notably, the state-of-the-art spin-coated FAPb_{0.5}Sn_{0.5}I₃ solar cells with an identical device structure using precursor solutions in a higher concentration (1.0 M) with the antisolvent processing method gave a record device efficiency of 11.6% based on a much thicker films (≈360 nm) than the one used here.^[17] The small difference indicates that our novel method is highly promising, having all the advantages of the scalable technique and the easy reproducibility than the antisolvent method.

It is interesting to note that our group has demonstrated superior efficiencies (16.2%) for the FA based alloyed system by substituting PEDOT:PSS with an anionic conjugated polymer PCP-Na.^[17] Considering this, we expect to be able to further improve the device performance using this polymer instead of the commonly employed PEDOT:PSS. Figure S20 (Supporting Information) reports devices of different areas fabricated with the LT method. Obviously, in larger areas devices the importance of cracks became more relevant. Importantly, this is a first step toward the fabrication of single crystalline-like SnPb alloyed perovskite solar cells using a scalable fabrication method. These initial results highlight that there is room for

future optimization of large area devices based on SnPb perovskites, as we forecasted recently.^[33] The optimization will go through limiting the crack formation or curing them after ion exchange. Importantly, other compositions (FA/MA mixtures) giving better results in spin coated devices should also be used using the template method in future.

3. Conclusion

Unlike traditional 3D mono-metal perovskites, Sn-alloyed binary perovskites with their competing crystallization of individual sublattice impose difficulties on obtaining films with ideal stoichiometry by employing scalable fabrication techniques. Here we have successfully proposed an approach to break the bottleneck by using a scalable approach based on a layered (2D perovskites)-template driven growth of 3D SnPb perovskites. By virtue of an in situ cation exchange reaction between PEA⁺ and FA⁺, the converted FA(Pb_{0.5}Sn_{0.5})I₃ film show a stoichiometric composition and a preferred orientation with the (100) planes parallel to the substrate. Owing to its low surface/volume ratio, the stability of the single-crystal-like binary perovskites is significantly enhanced even under various environmental conditions, when compared to that of the spin coated polycrystalline films obtained with a solution of similar molarity. We further identify that such high-quality film can work as an absorber for photovoltaic application. This work provides a sensible engineering approach for the further development of large-scale controlled growth of alloyed perovskites.

Supporting Information

Supporting Information is available from the Wiley Online Library or from the author.

Acknowledgements

The authors thank the kind technical support of Arjen Kamp and Teo Zaharia. J.X. and M.A.L. acknowledge the support from the Materials for Sustainability (Mat4Sus) program (739.017.005) of the Netherlands Organization for Scientific Research (NWO). The authors thank Dr. Simon Kahmann for help on interpreting Raman spectra. This work was part of the research program of the Foundation for Fundamental Research on Matter (FOM), which was part of the Netherlands Organization for Scientific Research (NWO). This is a publication of the FOM-focus Group "Next Generation Organic Photovoltaics," participating in the Dutch Institute for Fundamental Energy Research (DIFFER).

Conflict of Interest

The authors declare no conflict of interest.

Data Availability Statement

The data that support the findings of this study are available from the corresponding author upon reasonable request.

Keywords

2D template, highly crystalline, lead-tin perovskites, scalable fabrication, stability

Received: June 14, 2021

Revised: July 26, 2021

Published online: August 16, 2021

- [1] J.-P. Correa-Baena, M. Saliba, T. Buonassisi, M. Grätzel, A. Abate, W. Tress, A. Hagfeldt, *Science* **2017**, *358*, 739.
- [2] A. J. Jena, A. Kulkarni, T. Miyasaka, *Chem. Rev.* **2019**, *119*, 3036.
- [3] N.-G. Park, K. Zhu, *Nat. Rev. Mater.* **2020**, *5*, 333.
- [4] Best Research-Cell Efficiency Chart (NREL), <https://www.nrel.gov/pv/cell-efficiency.html> (accessed: November 2020).
- [5] J. Li, H.-L. Cao, W.-B. Jiao, Q. Wang, M. Wei, I. Cantone, J. Lü, A. Abate, *Nat. Commun.* **2020**, *11*, 310.
- [6] A. Abate, *Joule* **2017**, *1*, 659.
- [7] W. Ke, C. C. Stoumpos, M. Zhu, L. Mao, I. Spanopoulos, J. Liu, O. Y. Kontsevoi, M. Chen, D. Sarma, Y. Zhang, M. R. Wasielewski, M. G. Kanatzidis, *Sci. Adv.* **2017**, *3*, e1701293.
- [8] J. Xi, Z. Wu, B. Jiao, H. Dong, C. Ran, C. Piao, T. Lei, T.-B. Song, W. Ke, T. Yokoyama, X. Hou, M. G. Kanatzidis, *Adv. Mater.* **2017**, *29*, 1606964.
- [9] S. Shao, J. Liu, G. Portale, H.-H. Fang, G. R. Blake, G. H. ten Brink, L. J. A. Koster, M. A. Loi, *Adv. Energy Mater.* **2018**, *8*, 1702019.
- [10] X. Meng, Y. Wang, J. Lin, X. Liu, X. He, J. Barbaud, T. Wu, T. Noda, X. Yang, L. Han, *Joule* **2020**, *4*, 902.
- [11] K. Nishimura, M. A. Kamarudin, D. Hirotoni, K. Hamada, Q. Shen, S. Iikubo, T. Minemoto, K. Yoshino, S. Hayase, *Nano Energy* **2020**, *74*, 104858.
- [12] T. Leijtens, R. Prasanna, A. Gold-Parker, M. F. Toney, M. D. McGehee, *ACS Energy Lett.* **2017**, *2*, 2159.
- [13] D. Ricciarelli, D. Meggiolaro, F. Ambrosio, F. De Angelis, *ACS Energy Lett.* **2020**, *5*, 2787.
- [14] I. Celik, A. B. Phillips, Z. Song, Y. Yan, R. J. Ellingson, M. J. Heben, D. Apul, *Energy Environ. Sci.* **2017**, *10*, 1874.
- [15] A. Goyal, S. McKechnie, D. Pashov, W. Tumas, M. van Schilfgaarde, V. Stevanović, *Chem. Mater.* **2018**, *30*, 3920.
- [16] H.-H. Fang, S. Adjokatse, S. Shao, J. Even, M. A. Loi, *Nat. Commun.* **2018**, *9*, 243.
- [17] S. Shao, Y. Cui, H. Duim, X. Qiu, J. Dong, G. H. ten Brink, G. Portale, R. C. Chiechi, S. Zhao, J. Hou, M. A. Loi, *Adv. Mater.* **2018**, *30*, 1803703.
- [18] T. Kappel, T. S. Ripolles, K. Hamada, Y. Ogomi, T. Bessho, G. Kinoshita, J. Chantana, K. Yoshino, Q. Shen, T. Toyoda, T. Minemoto, T. N. Murakami, H. Segawa, S. Hayase, *Nano Lett.* **2018**, *18*, 3600.
- [19] R. Lin, K. Xiao, Z. Qin, Q. Han, C. Zhang, M. Wei, M. I. Saidaminov, Y. Gao, J. Xu, M. Xiao, A. Li, J. Zhu, E. H. Sargent, H. Tan, *Nat. Energy* **2019**, *4*, 864.
- [20] W. Ke, C. Chen, I. Spanopoulos, L. Mao, I. Hadar, X. Li, J. M. Hoffman, Z. Song, Y. Yan, M. G. Kanatzidis, *J. Am. Chem. Soc.* **2020**, *142*, 15049.
- [21] K. Xiao, R. Lin, Q. Han, Y. Hou, Z. Qin, H. T. Nguyen, J. Wen, M. Wei, V. Yeddu, M. I. Saidaminov, Y. Gao, X. Luo, Y. Wang, H. Gao, C. Zhang, J. Xu, J. Zhu, E. H. Sargent, H. Tan, *Nat. Energy* **2020**, *5*, 870.
- [22] L. E. Mundt, J. Tong, A. F. Palmstrom, S. P. Dunfield, K. Zhu, J. J. Berry, L. T. Schelhas, E. L. Ratcliff, *ACS Energy Lett.* **2020**, *5*, 3344.
- [23] D. Ramirez, K. Schutt, Z. Wang, A. J. Pearson, E. Ruggeri, H. J. Snaith, S. D. Stranks, F. Jaramillo, *ACS Energy Lett.* **2018**, *3*, 2246.

- [24] L. N. Quan, M. Yuan, R. Comin, O. Voznyy, E. M. Beauregard, S. Hoogland, A. Buin, A. R. Kirmani, K. Zhao, A. Amassian, D. H. Kim, E. H. Sargent, *J. Am. Chem. Soc.* **2016**, *138*, 2649.
- [25] L. Mao, C. C. Stoumpos, M. G. Kanatzidis, *J. Am. Chem. Soc.* **2019**, *141*, 1171.
- [26] J. Xi, I. Spanopoulos, K. Bang, J. Xu, H. Dong, Y. Yang, C. D. Malliakas, J. M. Hoffman, M. G. Kanatzidis, Z. Wu, *J. Am. Chem. Soc.* **2020**, *142*, 19705.
- [27] G. Grancini, M. K. Nazeeruddin, *Nat. Rev. Mater.* **2019**, *4*, 4.
- [28] S. Adjokatse, H.-H. Fang, H. Duim, M. A. Loi, *Nanoscale* **2019**, *11*, 5989.
- [29] N. Ahn, D.-Y. Son, I.-H. Jang, S. M. Kang, M. Choi, N.-G. Park, *J. Am. Chem. Soc.* **2015**, *137*, 8696.
- [30] W. Ke, I. Spanopoulos, Q. Tu, I. Hadar, X. Li, G. S. Shekhawat, V. P. Dravid, M. G. Kanatzidis, *J. Am. Chem. Soc.* **2019**, *141*, 8627.
- [31] M. He, B. Li, X. Cui, B. Jiang, Y. He, Y. Chen, D. O'Neil, P. Szymanski, M. A. El-Sayed, J. Huang, Z. Lin, *Nat. Commun.* **2017**, *8*, 16045.
- [32] S. Chen, X. Xiao, B. Chen, L. L. Kelly, J. Zhao, Y. Lin, M. F. Toney, J. Huang, *Sci. Adv.* **2021**, *7*, eabb2412
- [33] J. Xi, M. A. Loi, *ACS Energy Lett.* **2021**, *6*, 1803.